IEEE Photonics Journal
An IEEE Photonics Society Publication

Open Access

Link Gain and Pulse Width Broadening Evaluation of Non-Line-of-Sight Optical Wireless Scattering Communication Over Broad Spectra

Volume 9, Number 3, June 2017

Yu Sun
Chen Gong
Zhengyuan Xu
Yafeng Zhan

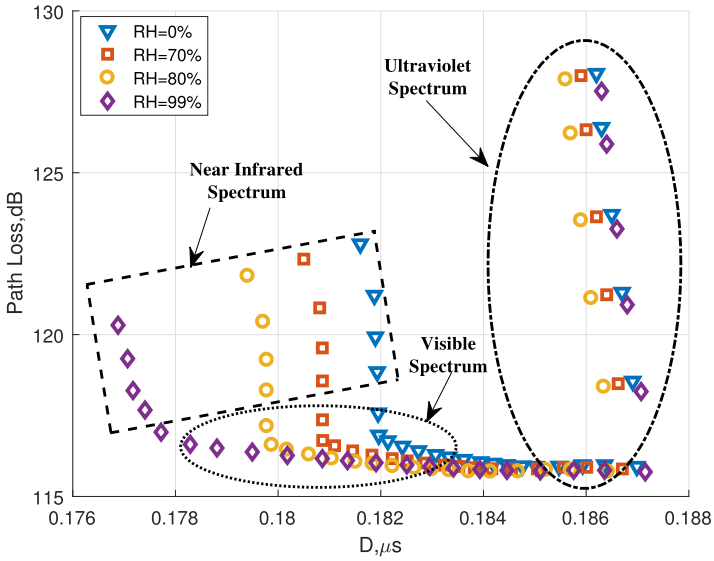

DOI: 10.1109/JPHOT.2017.2707468
1943-0655 © 2017 IEEE

IEEE photonics SOCIETY

IEEE

Link Gain and Pulse Width Broadening Evaluation of Non-Line-of-Sight Optical Wireless Scattering Communication Over Broad Spectra

Yu Sun,[1] Chen Gong,[2] Zhengyuan Xu,[2,3] and Yafeng Zhan

[1]Space Center, Tsinghua University, Beijing 100084, China
[2]Key Laboratory of Wireless-Optical Communications, Chinese Academy of Sciences, School of Information Science and Technology, University of Science and Technology of China, Hefei 230027, China
[3]Shenzhen Graduate School, Tsinghua University, Shenzhen 518055, China

DOI:10.1109/JPHOT.2017.2707468

Manuscript received April 18, 2017; revised May 17, 2017; accepted May 18, 2017. Date of publication June 1, 2017; date of current version June 8, 2017. This work was supported in part by the National Key Basic Research Program of China under Grant 2013CB329201, in part by the National Natural Science Foundation of China under Grant 61671263, in part by Tsinghua University Initiative Scientific Research Program under Grant 2013089244 and Grant 20161080057, and in part by the Shenzhen Peacock Plan under Grant 1108170036003286. Corresponding author: Yu Sun (e-mail: sunyu13@mails.tsinghua.edu.cn).

Abstract: In addition to large path loss, non-line-of-sight (NLOS) optical wireless scattering communication suffers time dispersion due to the multipath nature of the NLOS scattering channel. In this paper, the channel pulse delay spreads over broad spectra [0.2, 1.6] μm in polydisperse aerosols are investigated based on the Monte Carlo ray-tracing method. It is shown that the pulse delay spread first rises and then falls as the wavelength increases from deep ultraviolet to near-infrared spectrum. A comparison of pulse delay spread and path loss distributions over broad spectra is performed, which implies a tradeoff of channel bandwidth and power loss in the wavelength selection of NLOS optical scattering communication. The effects of relative humidity (RH) variations on NLOS optical scattering communication link are also studied, which indicate that RH variations do not significantly change the ultraviolet NLOS optical scattering communication link, but for near infrared spectrum, high RH condition can alleviate the large path loss and time dispersion and thus improve the NLOS optical scattering communication performance.

Index Terms: Free-space optical communication, non-line-of-sight, path loss, pulse delay spread, relative humidity.

1. Introduction

Non-Line-of-Sight (NLOS) optical wireless scattering communication is achieved via the light propagation by the scattering of air molecules and suspended aerosol particles. It can provide an alternative solution to the occasions where the transmitter (Tx) and receiver (Rx) are blocked by obstacles, or the direct line-of-sight link cannot be guaranteed due to application requirements. NLOS optical scattering communication system operates typically in the deep ultraviolet spectrum, and can be extended to visible and near infrared spectrum [1]–[3]. Because of its flexible operation, no electromagnetic radiation and potential broad spectra, NLOS optical scattering communication can

be employed as an alternative to conventional communication and has attracted extensive great attention in recent years [4]–[11].

In the literature, simulation [12], analytical [13], and experimental [14] approaches have been used to study the NLOS scattering channel characteristics. These studies demonstrate that NLOS optical scattering communication link suffers time dispersion due to the multipath nature of NLOS scattering channel. In addition to the inter-symbol interference (ISI) resulting from the pulse broadening effect, NLOS optical scattering communication link suffers large path loss due to the atmospheric scattering process. Ignoring the intensity fluctuation induced by turbulence, scattering and absorption are two major atmospheric effects on the channel pulse delay spread and path loss, and their effects depend on wavelength. Therefore, it is necessary to study the NLOS scattering channel characteristics across broad spectra, to give a reference of wavelength selection and examine the NLOS optical scattering communication performance across different wavelengths under different operating conditions.

The path loss over broad spectra under different communication ranges and visibilities (VIS) has been investigated in [1], [2], while the study of pulse delay spread over broad spectra has not been addressed. Beyond that, a monodisperse aerosol producible in the laboratory that contains particles with a uniform size is assumed in [1], [2]. However, as polydisperse colloidal systems, most aerosols in real life exhibit a range of particle sizes described by particle size distribution [15]. Therefore, the assumption in [1], [2] that aerosol particles with a uniform size may not be appropriate for most aerosols in real life. As shown in [1], [7], the aerosol number concentration, size distribution and refractive index essentially determine the scattering and absorption properties and the resulting NLOS scattering channel characteristics. The aerosol number concentration is indicated by visibility (VIS), while the size distribution shape and particle refractive index change with relative humidity (RH) [16]. Therefore, in addition to VIS, RH variations may also have impacts on the NLOS scattering channel properties and the resulting communication performance, which have not been investigated before.

In this paper, through the Monte-Carlo ray tracing method, we will comprehensively investigate the NLOS scattering channel pulse spread, path loss and the resulting communication performance over broad spectra [0.2, 1.6] μm in polydisperse aerosols, and the effects of RH variations on NLOS optical scattering communication link are also studied. The rest of this paper is organized as follows. In Section II, the general calculation formulas of aerosol scattering and absorption coefficients are introduced for particle size distribution with arbitrary shape, and the functions describing the effects of RH variations on aerosol size and refractive index are also presented. In Section III, through Monte-Carlo ray tracing method, the pulse delay spread, path loss and communication data rates are evaluated at different wavelengths, and the impacts of RH variations are investigated. Finally, Section IV provides the concluding remarks.

2. Atmospheric Properties Over Broad Spectra

2.1 Atmospheric Scattering and Absorption Parameters

In the light atmospheric transmission, the average distance a photon travels before being absorbed or scattered is determined by the absorption and scattering coefficient k_a and k_s [12]. The scattering (absorption) effect can be either caused by small air molecules or large size aerosols, which can be described by Rayleigh or Mie theory, respectively. Therefore, the total scattering (absorption) coefficient is the sum of molecule and aerosol scattering (absorption) coefficients, i.e., $k_s = k_s^{Ray} + k_s^{Mie}$ ($k_a = k_a^{Ray} + k_a^{Mie}$), where k_s^{Ray} and k_a^{Ray} are the molecule (Rayleigh) scattering and absorption coefficient, and k_s^{Mie} and k_a^{Mie} are the aerosol (Mie) scattering and absorption coefficient, respectively.

The composition of air molecules is relatively constant in low-altitude area; and the corresponding Rayleigh scattering coefficient k_s^{Ray} is given by [17]

$$k_s^{Ray} = \frac{24\pi^3}{\lambda^4 N_s} \frac{\left(m_s^2 - 1\right)^2}{\left(m_s^2 + 2\right)^2} \frac{6 + 3\delta}{6 - 7\delta}, \tag{1}$$

where $N_s = 2.54743 \times 10^{25}$ m^{-3} is the molecular number density for standard air; λ is the wavelength in unit of μm; δ is the depolarization factor, whose values at different wavelengths for standard air are listed in [18, Table 2]; m_s is the air refractive index and at sea level it can be given by [17]

$$(m_s - 1) \times 10^8 = 8060.51 + \frac{2480990}{132.274 - \lambda^{-2}} + \frac{17455.7}{39.32957 - \lambda^{-2}}. \tag{2}$$

The Rayleigh absorption coefficient k_a^{Ray} is a combination of different air-sourced gas absorptions, such as O_2, O_3, CO_2, etc. These gas absorptions of different wavelengths under specific atmospheric condition can be obtained through widely used atmospheric radiation transport model - MODTRAN, as shown in [7].

Based on the Mie theory, the Mie scattering and absorption coefficients with particle size distribution $n(r)$ of arbitrary shape can be expressed as

$$\begin{cases} k_s^{Mie} = \int_0^\infty \pi r^2 Q_{sca}(r, \lambda, m)\, n(r)\, dr \\ k_a^{Mie} = \int_0^\infty \pi r^2 Q_{abs}(r, \lambda, m)\, n(r)\, dr \end{cases}, \tag{3}$$

where r is the particle radius; Q_{sca} and Q_{abs} are respectively the scattering and absorption efficiency and can be obtained by [19]

$$\begin{cases} Q_{sca}(r, \lambda, m) = \dfrac{2}{x^2} \sum_{n=1}^{\infty} (2n+1)\left(|a_n|^2 + |b_n|^2\right) \\ Q_{abs}(r, \lambda, m) = \dfrac{2}{x^2}\left[\sum_{n=1}^{\infty} (2n+1)\,\mathrm{Re}(a_n + b_n) - \sum_{n=1}^{\infty} (2n+1)\left(|a_n|^2 + |b_n|^2\right)\right] \end{cases}, \tag{4}$$

in which a_n and b_n are the functions of size parameter $x = 2\pi r/\lambda$ and particle complex refractive index m [19]

$$\begin{cases} a_n = \dfrac{m\psi_n(mx)\psi_n(x) - \psi_n(x)\psi_n(mx)}{m\psi_n(mx)\xi'_n(x) - \xi_n(x)\psi_n(mx)} \\ b_n = \dfrac{\psi_n(mx)\psi_n(x) - m\psi_n(x)\psi_n(mx)}{\psi_n(mx)\xi'_n(x) - m\xi_n(x)\psi_n(mx)} \end{cases}. \tag{5}$$

Here $\psi_n(x) = x j_n(x)$ and $\xi_n(x) = x h_n^{(1)}(x)$, where $j_n(x)$ and $h_n^{(1)}(x)$ are respectively the spherical Bessel function and spherical first kind Hankel function.

When a photon is scattered by air molecule (Rayleigh scattering) or aerosol particle (Mie scattering), the deflection angle θ_s is determined by the angular distribution of scattering, namely the scattering phase function $p(\theta_s)$. The Rayleigh scattering phase function can be given by [17]

$$p_{ray}(\theta_s) = \frac{3\left[1 + 3\gamma + (1-\gamma)\cos^2\theta_s\right]}{16\pi(1+2\gamma)}, \tag{6}$$

in which $\gamma = \delta/(2-\delta)$ is a wavelength dependent parameter. The Mie scattering phase function over broad spectra can be approximated with the Neer-Sandri function [20]

$$p_{mie}(\theta_s) = \frac{1-g^2}{4\pi}\left[\frac{1}{(1+g^2-2g\cos\theta_s)^{3/2}} + \frac{g\left(3\cos^2\theta_s - 1\right)}{0.286(1+g^2+0.286g)^{5/2}}\right]. \tag{7}$$

Here g is the asymmetric factor and can be expressed as

$$g = \frac{\int_0^\infty G(r, \lambda, m)\, n(r)\, dr}{\int_0^\infty n(r)\, dr}, \tag{8}$$

where G is obtained by [20]

$$G(r, \lambda, m) = \frac{4}{x^2 Q_{sca}} \sum_{n=1}^{\infty}\left[\frac{n(n+2)}{n+1}\mathrm{Re}\left(a_n a_{n+1}^* + b_n b_{n+1}^*\right) + \frac{2n+1}{n(n+1)}\mathrm{Re}\left(a_n b_n\right)\right]. \tag{9}$$

Considering the joint effect of Rayleigh and Mie scattering, the total scattering phase function $p(\theta_s)$ is expressed as the weighted sum of the Rayleigh and Mie scattering phase functions

$$p(\theta_s) = \frac{k_s^{Ray}}{k_s} p_{ray}(\theta_s) + \frac{k_s^{Mie}}{k_s} p_{mie}(\theta_s). \tag{10}$$

2.2 Effects of Relative Humidity Variations on Aerosol Properties

From the formulas above, we can see that the aerosol scattering and absorption effects are determined by the size of aerosol and particle refractive index. The basic effect of RH variations on the aerosol is that as the RH increases, the water vapor concentrates around the existing aerosol particles. Such concentrating water vapor increases the size of aerosol and thus changes the effective refractive index. As a result, the aerosol scattering and absorption properties will be correspondingly modified.

According to [16], the particle radius r is related to RH by

$$r(a_w) = r_0 \left[1 + \rho \frac{M_w(a_w)}{M_0}\right]^{1/3}, \tag{11}$$

where r_0 is the dry particle radius in unit of μm; ρ is the particle relative density; a_w is the water activity related to RH

$$a_w = \mathrm{RH} \cdot \exp\left(\frac{-0.001056}{r(a_w)}\right); \tag{12}$$

$M_w(a_w)$ and M_0 are respectively the mass of condensed water and dry particle; and the measurements of $M_w(a_w)/M_0$ versus a_w for various types of natural aerosol are shown in [16, Table 3].

Once the wet aerosol particle radius is determined by (11)-(12), the complex refractive index m is calculated as the volume weighted average of the refractive indices of water m_w and dry aerosol substance m_0, given by

$$m = m_w + (m_0 - m_w)\left[\frac{r_0}{r(a_w)}\right]^3. \tag{13}$$

3. Simulation Results and Analysis

In this section, through Monte-Carlo ray tracing method, we present the numerical results of pulse delay spread over broad spectra under different communication ranges, and the maximum communication data rates at a given target bit error rate (BER) threshold for different wavelengths. The effects of RH variations on NLOS scattering channel characteristics and the resulting communication performance are also presented.

The NLOS optical scattering communication system geometry is illustrated in Fig. 1, where R is the range between Tx and Rx, θ_T is the Tx half beam divergence, θ_R is the Rx half field of view angle, β_T and β_R are respectively the elevation angle of Tx and Rx. The geometry parameters in simulation are set to be $(\theta_T, \theta_R) = (0.4\ \mathrm{mrad}, 15^\circ)$ and $(\beta_T, \beta_R) = (20^\circ, 20^\circ)$, and the effective detection area of Rx is 1.77 cm^2.

According to the experimental measurements in [21], the aerosol particle size distribution can be expressed as the sum of two log-normal distributions

$$n(r) = \sum_{i=1}^{2} \left(\frac{N_i}{r \cdot \ln(10) \cdot \sigma_i \sqrt{2\pi}}\right) \exp\left\{-\frac{1}{2}\left[\frac{\ln(r/r_i)}{\ln(10) \cdot \sigma_i}\right]^2\right\}, \tag{14}$$

where σ_i is the distribution width parameter, r_i is the mode radius and N_i is the number density with r_i.

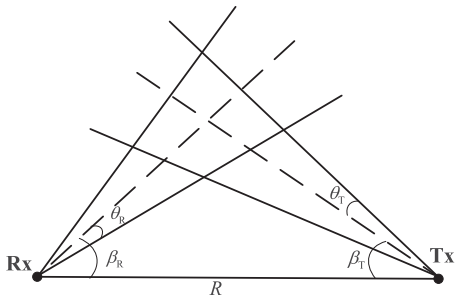

Fig. 1. Structure of NLOS optical scattering communication link.

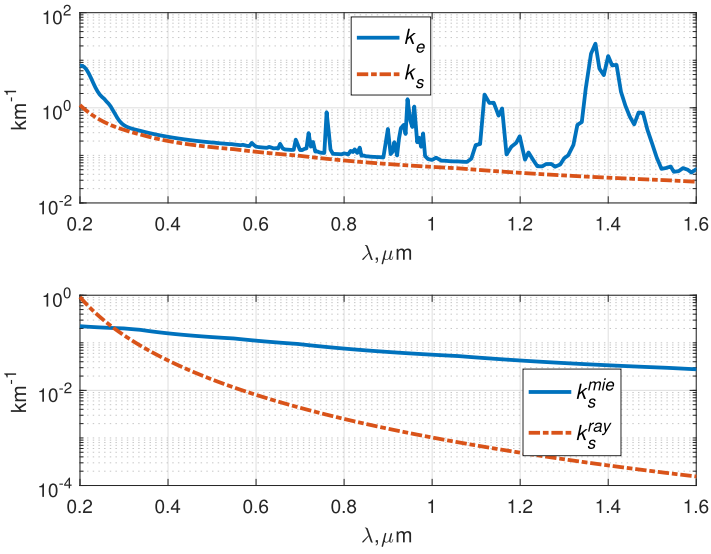

Fig. 2. Atmospheric coefficients versus wavelength (VIS = 23 km, RH = 80%).

To give an accurate representation of the chemical and optical properties of the aerosol particles in urban region, a typical urban aerosol model is adopted, which is a mixture of 20% soot-like aerosol and 80% rural aerosol (the rural aerosol is composed of 70% water soluble material and 30% dust like aerosol) [21]. The temperature condition is set to be 15 °C (1976 US standard model temperature at sea level), and the relation of temperature and relative humidity is specified in (5) of [22]. The size distribution parameters and refractive indices of urban aerosol model, as a function of wavelength, VIS and RH, are provided in [23, Tables 2, 5, and 9].

3.1 Pulse Delay Spread Over Broad Spectra

To evaluate the pulse delay spread over broad spectra, the first step is to determine the atmospheric parameters at different wavelengths. The calculation results of atmospheric coefficients versus wavelength for VIS = 23 km (normal days) and RH = 80% (moderate humidity) are presented in Fig. 2, where k_e is the extinction coefficient as the sum of scattering and absorption coefficients, i.e., $k_e = k_s + k_a$.

As shown in Fig. 2, except for some singularities due to the absorption by air constituents, k_e falls sharply as the wavelength increases from deep ultraviolet to visible spectrum, and varies gently from visible to near infrared band. We can also find in Fig. 2 that, both k_s^{Ray} and k_s^{Mie} decrease with wavelength, with a crossover between k_s^{Ray} and k_s^{Mie} curves. This phenomenon indicates that as the

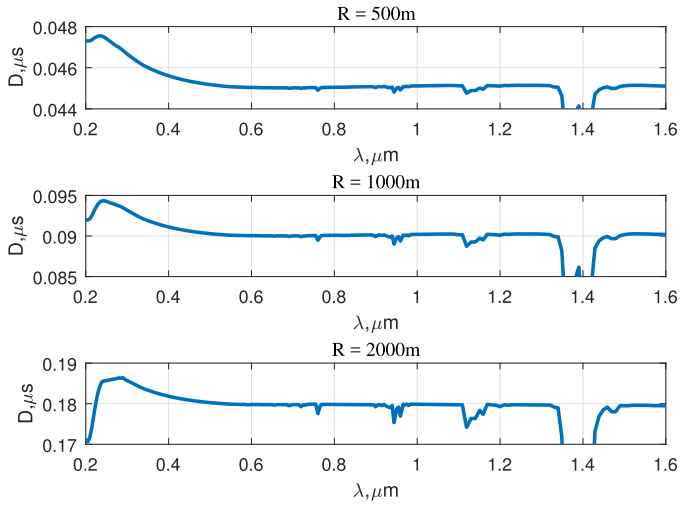

Fig. 3. Delay spread versus wavelength under different communication ranges (VIS = 23 km, RH = 80%).

wavelength increases, the dominant scattering changes from Rayleigh scattering to Mie scattering, implying that a better scattering directivity can be achieved.

As a parameter to quantify the time-dispersive property of NLOS scattering channel, the root mean square delay spread D is computed by [24]

$$D = \left[\frac{\int (t - \bar{t})^2 h(t)\, dt}{\int h(t)\, dt} \right]^{1/2}, \tag{15}$$

where $\bar{t}$ is the mean delay

$$\bar{t} = \frac{\int t h(t)\, dt}{\int h(t)\, dt}; \tag{16}$$

$h(t)$ is the channel impulse response (CIR) and can be obtained by Monte-Carlo ray-tracing method [12]. Applying the atmospheric coefficients in Fig. 2 to Monte-Carlo ray-tracing method, the results of D versus wavelength under different communication ranges are presented in Fig. 3.

We can see from Fig. 3 that the pulse delay spread first rises and then falls with wavelength. This phenomenon can be explained as follows. According to the closed-form CIR expression in [13], k_e and $p(\theta_s)$ are the two main wavelength dependent effects on the decay rate of CIR. The CIR decays slowly as k_e decreases. As a result, the delay spread rises first due to the sharp fall of k_e from deep ultraviolet to visible spectrum. As the wavelength increases to visible or near infrared band, due to the gentle variation of k_e, the effect of $p(\theta_s)$ becomes dominant, and a better scattering directivity will induce a lower CIR delay spread. As a result, the delay spread falls due to the higher Mie scattering contribution to the total scattering at longer wavelengths. We can also find in Fig. 3 that the pulse delay spread increases with communication range, since longer communication range will result in a lager NLOS scattering volume.

For comparison, the curves of pulse delay spread and path loss versus wavelength are illustrated in Fig. 4. The inverse relation of the two metrics versus wavelength can be observed from Fig. 4. This phenomenon can be explained through the closed-form expressions of CIR $h(t)$ [13] and path loss PL [8], which can be written as follows for clarity

$$\begin{cases} h(t) = \mathrm{A} \cdot k_s \cdot \mathrm{B}(t) \cdot \exp(-k_e \cdot c \cdot t) \cdot p[\theta_s(t)] \\ \mathrm{PL} = \alpha \cdot k_s^{-1} \cdot R \cdot \exp(k_e \cdot \beta \cdot R) \cdot \left[p\left(\theta_{s,\xi}\right) \right]^{-1} \end{cases}, \tag{17}$$

where c is the speed of light, A, B, α and β are the functions of system geometries.

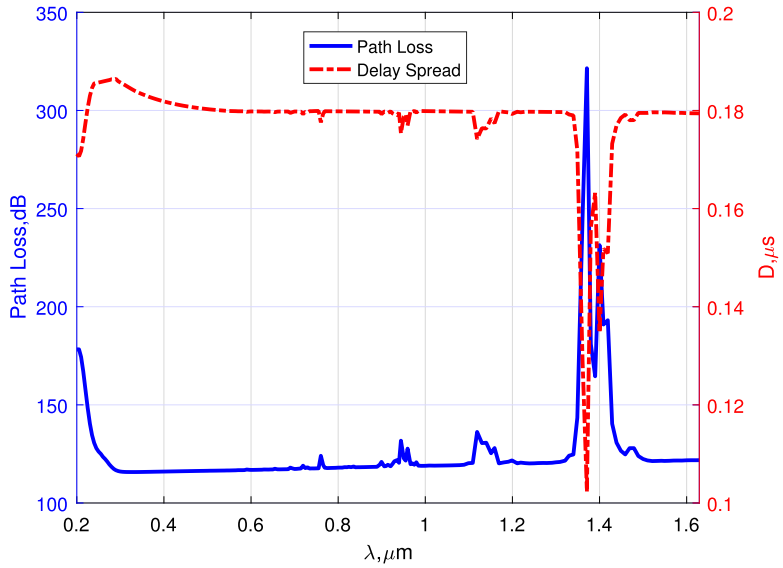

Fig. 4. Delay spread and path loss over broad spectra (VIS = 23 km, RH = 80%, R = 2 km).

As shown in (17), the path loss decreases and CIR decays slowly as k_e decreases. Therefore, the path loss first falls while delay spread rises because of the sharp fall of k_e from deep ultraviolet to visible spectrum. As k_e varies gently from visible to near infrared band, the scattering factors become dominant in the path loss and CIR. Since k_s decreases from visible to near infrared band, the path loss begins to rise while the delay spread falls due to the larger Mie scattering portion in the total scattering. As will be shown later, the negative correlation between the pulse delay spread and the path loss over broad spectra still exists under various RH conditions.

The results in Fig. 4 reveal a tradeoff of channel bandwidth and power loss in the wavelength selection of NLOS optical scattering communication. For example, in deep ultraviolet band, the path loss decreases with wavelength but the pulse delay spread increases. As a result, in ultraviolet NLOS optical scattering communication system, a communication approach that can better deal with the delay spread is preferred for the wavelength with lower path loss.

3.2 Effects of Relative Humidity Variations on NLOS Scattering Channel

The effects of RH variations on the atmospheric parameters over broad spectra are illustrated in Fig. 5. The RH variations have little impact on the scattering and absorption properties in deep ultraviolet spectrum. But for longer wavelength spectra, except for the wavelengths sensitive to the water vapor absorption, k_a decreases and k_s^{Mie} increases with the growth of RH, which can be attributed to higher concentration of large size aerosol particles under high RH condition.

Simulation results of path loss and pulse delay spread over broad spectra under different RH conditions are respectively shown in Figs. 6 and 7. We can see from Fig. 6 that for the wavelengths from visible light to near infrared spectrum, except for the singularities due to absorption by water vapor, high RH condition can decrease the path loss; and as the wavelength increases, the effects of RH variations on path loss become more significant. We can find in Fig. 7 that for visible and near infrared spectrum, high RH condition can help to decrease the pulse spread, which can be attributed to larger Mie scattering contribution to the total scattering under high RH condition.

The explanations of the conclusions in the above simulation results are given as follows. As shown in [19], the aerosol scattering and absorption efficiencies depend on the ratio of particle radius to the wavelength, and reach extreme values for the wavelength comparable to the particle radius. From the [23, Figs. 3, 6, and 9] which illustrate the aerosol number distributions for various aerosol

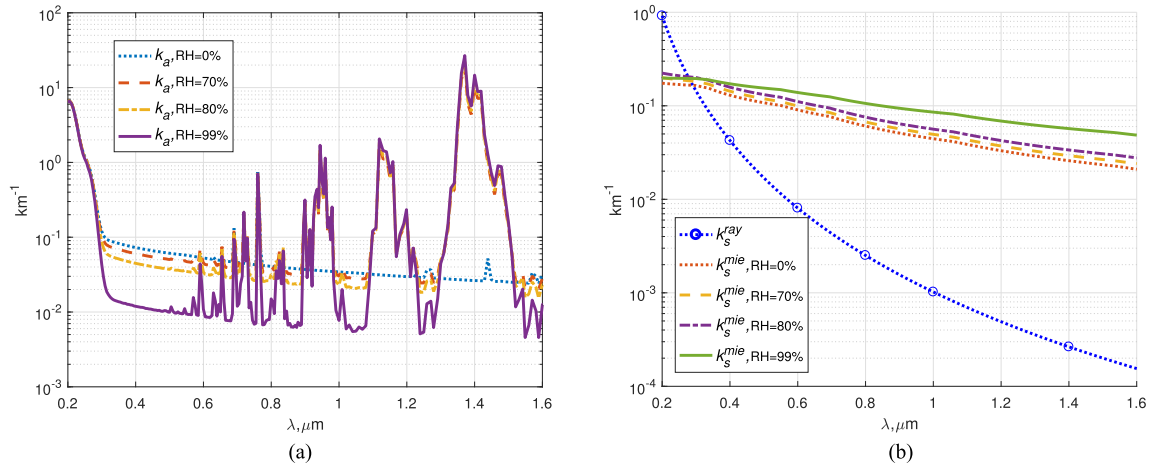

Fig. 5. Absorption coefficient (a) and scattering coefficient (b) versus wavelength under various RH conditions (VIS = 23 km).

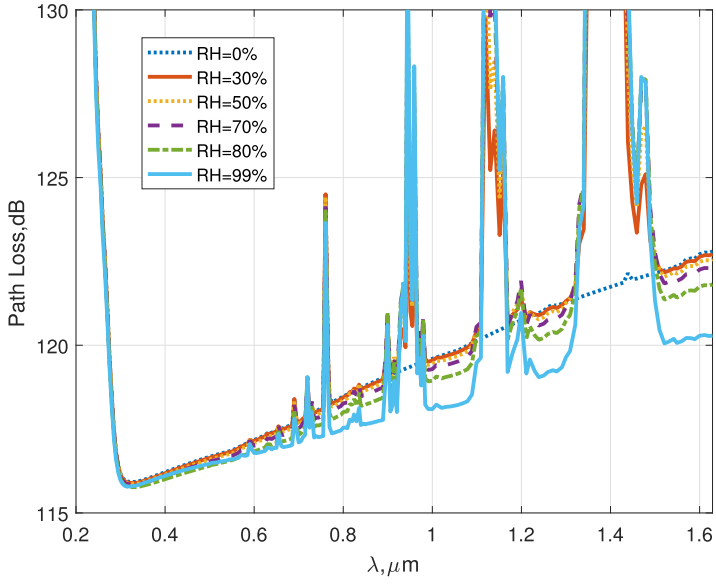

Fig. 6. Path loss versus wavelength under different RH conditions (VIS = 23 km, R = 2 km).

models under different RH, we will note that for all the aerosol models the relative numbers of large size particles increase significantly with increasing RH. This leads to a corresponding larger impact on the scattering and absorption properties of the long wavelength spectra than short wavelengths. Since the aerosol scattering efficiency reaches maximum for the wavelength comparable to the particle radius, the k_s^{Mie} and k_s for long wavelength spectra will increase with the growth of RH, due to the higher concentration of large size aerosol particles under high RH condition. This leads to more photons arrival at Rx through scattering and corresponding lower path loss for long wavelength spectra under high RH condition. As shown in Fig. 5, the contribution of Mie scattering to the total scattering increases with the growth of RH, which implies a better scattering directivity can be achieved and helps to decrease the pulse delay spread for long wavelength spectra under high RH condition.

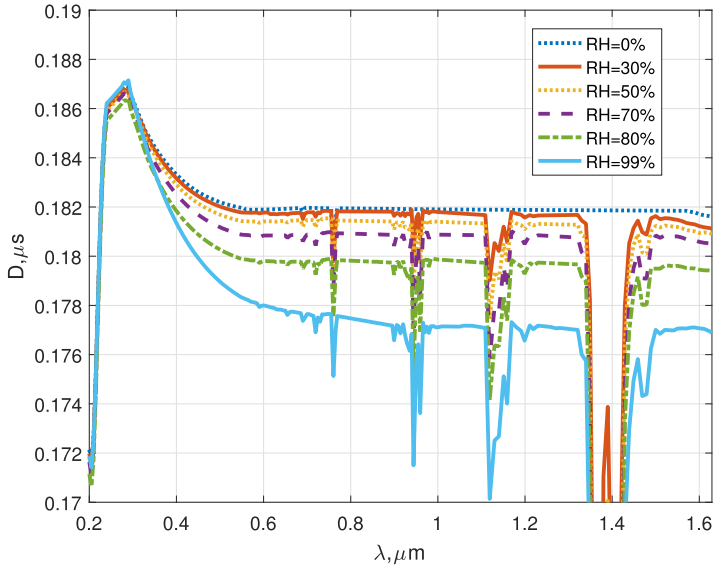

Fig. 7. Delay spread versus wavelength under different RH conditions (VIS = 23 km, R = 2 km).

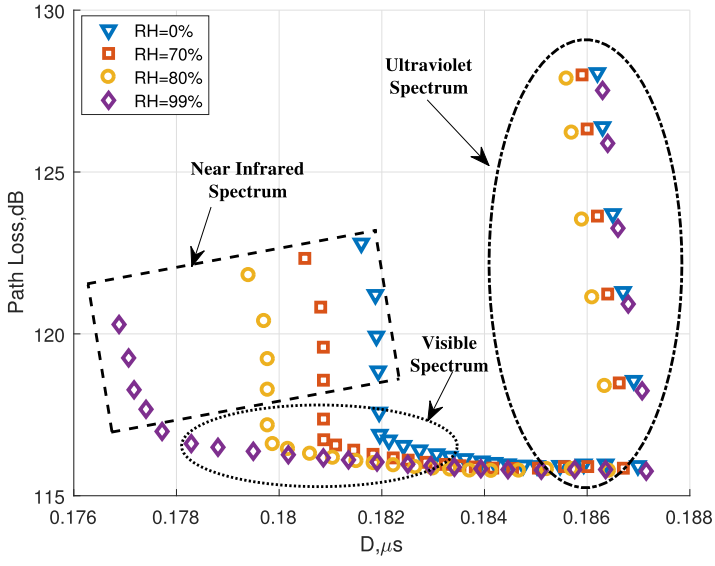

Fig. 8. Relations of path loss and delay spread over broad spectra under various RH conditions (VIS = 23 km, R = 2 km).

The relations of path loss and pulse delay spread distributions over broad spectra under different RH conditions are presented in Fig. 8, where the negative correlation between the path loss and pulse delay spread can be observed in ultraviolet, visible and near infrared spectrum.

3.3 Communication Performance Over Broad Spectra

Eight representative wavelengths (266, 405, 450, 532, 635, 660, 1064, 1550) nm are selected from deep ultraviolet to near infrared spectrum, to compute the maximum communication data rates at a given BER threshold for different optical spectra under various RH conditions. The discrete-time NLOS optical scattering communication channel model [24] is adopted, where the ISI induced by

TABLE 1
Background Irradiances at Different Wavelengths Under Various RH Conditions

Wavelength (nm)	Background Irradiance ($W/m^2/\mu m$)		
	RH = 0%	RH = 80%	RH = 99%
266	3.7×10^{-7}	3.7×10^{-7}	3.7×10^{-7}
405	209.15	209.15	209.15
450	306.10	306.10	306.10
532	311.18	311.18	311.18
635	289.14	289.14	289.14
660	281.07	281.07	281.07
1064	139.14	138.82	138.74
1550	56.83	56.64	56.62

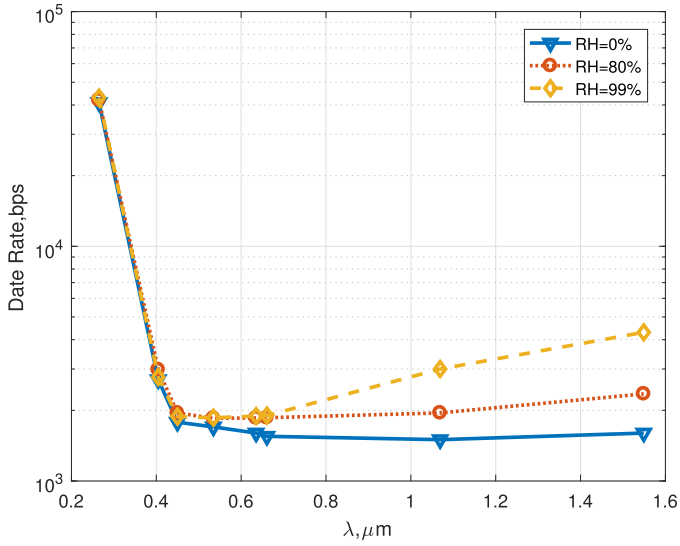

Fig. 9. The maximum communication data rates at different wavelengths under various RH conditions (VIS = 23 km, R = 1 km).

pulse delay spread is considered. In simulation, the total efficiency of optical filter and detector is set to be 6%, and the dark current noise is 10 count/s. Considering the optical devices available in practice, the ultraviolet optical filter bandwidth is set to be 15 nm and transmitted power is 200 mW, while for the other seven wavelengths, the filter bandwidth and transmitted power are respectively set to be 1 nm and 4 W.

The background irradiances of different wavelengths at day time are also included. Using the solar spectral model in [25], a day of spring and a neutral time of 9 o'clock in the morning are selected, and the corresponding solar elevation angle is set to be 20°. The corresponding total background irradiances for the eight wavelengths under different RH conditions are listed in Table I.

Fig. 9 presents the simulation results of maximum communication data rates at a given BER threshold as 10^{-4} for the eight wavelengths under different RH conditions. The on-off keying (OOK) modulation is adopted, and the communication range is 1 km and VIS = 23 km.

We can find in Fig. 9 that, though there are advantages of larger transmitted power and lower attenuation in the long range scattering transmission of visible and infrared spectrum, the maximum data rates of (405, 450, 532, 635, 660, 1064, 1550) nm are much lower than that of 266 nm, which can be attributed to the considerably higher background irradiance in the visible and infrared spectrum than that in the deep ultraviolet spectrum. Thus, in order to improve the visible or near infrared NLOS optical scattering communication performance, the high background irradiance needs to be properly filtered, for example, by means of an ultra-narrow bandwidth filter. We can also see from Fig. 9 that the maximum data rate increases with RH for long wavelengths especially for the near infrared spectrum, which indicates that operating under high RH condition can help to improve the near infrared NLOS optical scattering communication performance.

4. Conclusion

In this paper, based on Monte-Carlo ray tracing method, the NLOS scattering channel properties and the resulting communication performance over broad spectra in polydisperse aerosols are investigated. Simulation results reveal that the pulse delay spread first increases and then decreases with the wavelength from deep ultraviolet to near infrared spectrum. The pulse delay spread and path loss distributions over broad spectra show a negative correlation across different wavelengths. Furthermore, the effects of RH variations on NLOS optical scattering communication link are also studied. Results indicate that RH variations have little impact on the ultraviolet NLOS optical scattering communication link; but for near infrared spectrum, high RH condition can decrease the pulse delay spread and path loss, and thus improve the NLOS optical scattering communication performance.

References

[1] W. Liu, D. Zou, and Z. Xu, "Modeling of optical wireless scattering communication channels over broad spectra," *J. Opt. Soc. Amer. A*, vol. 32, no. 3, pp. 486–490, Mar. 2015.

[2] C. Xu and H. Zhang, "Channel analyses over wide optical spectra for long-range scattering communication," *IEEE Commun. Lett.*, vol. 19, no. 2, pp. 187–190, Feb. 2015.

[3] S. Zhang *et al.*, "Attenuation analysis of long-haul NLOS atmospheric optical scattering communication," *Opt. Laser Technol.*, vol. 80, pp. 51–55, Jun. 2016.

[4] Z. Ghassemlooy, S. Arnon, M. Uysal, Z. Xu, and J. Cheng, "Emerging optical wireless communications-advances and challenges," *IEEE J. Sel. Areas Commun.*, vol. 33, no. 9, pp. 1738–1749, Sep. 2015.

[5] R. J. Drost and B. M. Sadler, "Survey of ultraviolet non-line-of-sight communications," *Semicond. Sci. Technol.*, vol. 29, no. 8, Aug. 2014, Art. no. 084006.

[6] I. S. Ansari, F. Yilmaz, and M.-S. Alouini, "Performance analysis of free-space optical links over Malaga (M) turbulence channels with pointing errors," *IEEE Trans. Wireless Commun.*, vol. 15, no. 1, pp. 91–102, Jan. 2016.

[7] C. Xu, H. Zhang, and J. Cheng, "Effects of haze particles and fog droplets on NLOS ultraviolet communication channels," *Opt. Exp.*, vol. 23, no. 18, pp. 23259–23269, Sep. 2015.

[8] P. Wang, H. Zhang, and Z. Xu, "Simplified model and experimental validation for ultraviolet single-scattering channels," *Chin. Opt. Lett.*, vol. 13, no. 8, Aug. 2015, Art. no. 080603.

[9] P. Wang and Z. Xu, "Characteristics of ultraviolet scattering and turbulent channels," *Opt. Lett.*, vol. 38, no. 15, pp. 2773–2775, Jan. 2013.

[10] T. Liu, P. Wang, and H. Zhang, "Performance analysis of non-line-of-sight ultraviolet communication through turbulence channel," *Chin. Opt. Lett.*, vol. 13, no. 4, Apr. 2015, Art. no. 040601.

[11] D. Zou and Z. Xu, "Information security risks outside the laser beam in terrestrial free-space optical communication," *IEEE Photon. J.*, vol. 8, no. 5, Oct. 2016, Art. no. 7804809.

[12] R. J. Drost, T. J. Moore, and B. M. Sadler, "UV communications channel modeling incorporating multiple scattering interactions," *J. Opt. Soc. Amer. A*, vol. 28, no. 4, pp. 686–695, Apr. 2011.

[13] Y. Sun and Y. Zhan, "Closed-form impulse response model of non-line-of-sight single-scatter propagation," *J. Opt. Soc. Amer. A*, vol. 33, no. 4, pp. 752–757, Apr. 2016.

[14] G. Chen, Z. Xu, and B. M. Sadler, "Experimental demonstration of ultraviolet pulse broadening in short-range non-line-of-sight communication channels," *Opt. Exp.*, vol. 18, no. 10, pp. 10500–10509, May 2010.

[15] W. C. Hinds, *Aerosol Technology: Properties, Behavior, and Measurement of Airborne Particles*. New York, NY, USA: Wiley, 2012.

[16] G. Hänel, "The properties of atmospheric aerosol particles as functions of the relative humidity at thermodynamic equilibrium with the surrounding moist air," *Adv. Geophys.*, vol. 19, pp. 73–188, 1976.

[17] A. Bucholtz, "Rayleigh-scattering calculations for the terrestrial atmosphere," *Appl. Opt.*, vol. 34, no. 15, pp. 2765–2773, May 1995.

[18] C. Tomasi, V. Vitale, B. Petkov, A. Lupi, and A. Cacciari, "Improved algorithm for calculations of Rayleigh-scattering optical depth in standard atmospheres," *Appl. Opt.*, vol. 44, no. 16, pp. 3320–3341, Jun. 2005.
[19] C. F. Bohren and D. R. Huffman, *Absorption and Scattering of Light by Small Particles*. Hoboken, NJ, USA: Wiley, 2007.
[20] E. S. Fishburne, M. E. Neer, and G. Sandri, "Voice communication via scattered ultraviolet radiation. volume 1," Aeronaut. Res. Assoc. Princeton, Princeton, NJ, USA, Tech. Rep. 274, 1976.
[21] S. B. Carr, "The aerosol models in MODTRAN: incorporating selected measurements from Northern Australia," Defence Sci. Technol. Org., Canberra, Australia, Tech. Rep. DSTO-TR-1803, 2005.
[22] S. A. Al-Gailani, A. B. Mohammad, M. S. Islam, U. U. Sheikh, and R. Q. Shaddad, "Tropical temperature and humidity modeling for free space optical link," *J. Opt.*, vol. 45, no. 1, pp. 87–91, 2016.
[23] E. P. Shettle and R. W. Fenn, "Models for the aerosols of the lower atmosphere and the effects of humidity variations on their optical properties," Air Force Geophys. Lab., Wright-Patterson Air Force Base, OH, USA, Tech. Rep. AFGL-TR-79-0214, 1979.
[24] M. A. El-Shimy and S. Hranilovic, "Binary-input non-line-of-sight solar-blind uv channels: Modeling, capacity and coding," *IEEE/OSA J. Opt. Commun. Netw.*, vol. 4, no. 12, pp. 1008–1017, Dec. 2012.
[25] R. E. Bird and C. Riordan, "Simple solar spectral model for direct and diffuse irradiance on horizontal and tilted planes at the Earth's surface for cloudless atmospheres," *J. Climate Appl. Meteorol.*, vol. 25, no. 1, pp. 87–97, Jan. 1986.